Optimization and analysis of 3D nanostructures for power-density enhancement in ultra-thin photovoltaics under oblique illumination

Bing Shen, Peng Wang, and Rajesh Menon*

Department of Electrical and Computer Engineering, University of Utah, Salt Lake City, Utah 84112, USA
[*]rmenon@eng.utah.edu

Abstract: Nanostructures have the potential to significantly increase the output power-density of ultra-thin photovoltaic devices by scattering incident sunlight into resonant guided modes. We applied a modified version of the direct-binary-search algorithm to design such nanostructures in order to maximize the output power-density under oblique-illumination conditions. We show that with appropriate design of nanostructured cladding layers, it is possible for a 10nm-thick organic absorber to produce an average peak power-density of 4mW/cm^2 with incident polar angle ranging from $-90°$ to $90°$ and incident azimuthal angle ranging from $-23.5°$ to $23.5°$. Using careful modal and spectral analysis, we further show that an optimal trade-off of absorption at $\lambda \sim 510$nm among various angles of incidence is essential to excellent performance under oblique illumination. Finally, we show that the optimized device with no sun tracking can produce on an average 7.23 times more energy per year than that produced by a comparable unpatterned device with an optimal anti-reflection coating.

References and links

1. H. Hoppe and N. S. Sariciftci, "Organic solar cells: An overview," J. Mater. Res. **19**(07), 1924–1945 (2004).
2. C. Min, J. Li, G. Veronis, J. Lee, S. Fan, and P. Peumans, "Enhancement of optical absorption in thin-film organic solar cells through the excitation of plasmonic modes in metallic gratings," Appl. Phys. Lett. **93**(7), 073307 (2008).
3. M. Kaltenbrunner, M. S. White, E. D. Głowacki, T. Sekitani, T. Someya, N. S. Sariciftci, and S. Bauer, "Ultrathin and lightweight organic solar cells with high flexibility," Nat Commun **3**, 770 (2012).
4. T. L. Benanti and D. Venkataraman, "Organic solar cells: an overview focusing on active layer morphology," Photosynth. Res. **87**(1), 73–81 (2006).
5. J. L. Brédas, J. E. Norton, J. Cornil, and V. Coropceanu, "Molecular understanding of organic solar cells: the challenges," Acc. Chem. Res. **42**(11), 1691–1699 (2009).
6. P. Wang and R. Menon, "Optimization of periodic nanostructures for enhanced light-trapping in ultra-thin photovoltaics," Opt. Express **21**(5), 6274–6285 (2013).
7. A. Raman, Z. Yu, and S. Fan, "Dielectric nanostructures for broadband light trapping in organic solar cells," Opt. Express **19**(20), 19015–19026 (2011).
8. K. X. Wang, Z. Yu, V. Liu, Y. Cui, and S. Fan, "Absorption enhancement in ultrathin crystalline silicon solar cells with antireflection and light-trapping nanocone gratings," Nano Lett. **11**(2), 661–665 (2011).
9. J. R. Tumbleston, D.-H. Ko, E. T. Samulski, and R. Lopez, "Absorption and quasiguided mode analysis of organic solar cells with photonic crystal photoactive layers," Opt. Express **17**(9), 7670–7681 (2009).
10. D.-H. Ko, J. R. Tumbleston, L. Zhang, S. Williams, J. M. DeSimone, R. Lopez, and E. T. Samulski, "Photonic crystal geometry for organic solar cells," Nano Lett. **9**(7), 2742–2746 (2009).
11. N. C. Lindquist, W. A. Luhman, S.-H. Oh, and R. J. Holmes, "Plasmonic nanocavity arrays for enhanced efficiency in organic photovoltaic cells," Appl. Phys. Lett. **93**(12), 123308 (2008).
12. H. Shen, P. Bienstman, and B. Maes, "Plasmonic absorption enhancement in organic solar cells with thin active layers," J. Appl. Phys. **106**(7), 073109 (2009).
13. A. E. Ostfeld and D. Pacifici, "Plasmonic concentrators for enhanced light absorption in ultrathin film organic photovoltaics," Appl. Phys. Lett. **98**(11), 113112 (2011).

14. S. Sandhu, Z. Yu, and S. Fan, "Detailed balance analysis of nanophotonic solar cells," Opt. Express **21**(1), 1209–1217 (2013).
15. P. Wang and R. Menon, "Simulation and optimization of 1-D periodic dielectric nanostructures for light-trapping," Opt. Express **20**(2), 1849–1855 (2012).
16. A. Chutinan and S. John, "Light trapping and absorption optimization in certain thin-film photonic crystal architectures," Phys. Rev. A **78**(2), 023825 (2008).
17. A. Lenz, H. Kariis, A. Pohl, P. Persson, and L. Ojamae, "The electronic structures and reflectivity of PEDOT:PSS from density functional theory," Chem. Phys. **384**(1–3), 44–51 (2011).
18. M. Leclerc and A. Najari, "Organic thermoelectrics: Green energy from a blue polymer," Nat. Mater. **10**(6), 409–410 (2011).
19. P. Wang and R. Menon, "Optimization of generalized dielectric nanostructures for enhanced light trapping in thin-film photovoltaics via boosting the local density of optical states," Opt. Express **22**(S1), A99–A110 (2014).
20. G. Kim, J. A. Domínguez-Caballero, and R. Menon, "Design and analysis of multi-wavelength diffractive optics," Opt. Express **20**(3), 2814–2823 (2012).
21. D. M. Callahan, J. N. Munday, and H. A. Atwater, "Solar cell light trapping beyond the ray optic limit," Nano Lett. **12**(1), 214–218 (2012).
22. Y. Yuan, T. J. Reece, P. Sharma, S. Poddar, S. Ducharme, A. Gruverman, Y. Yang, and J. Huang, "Efficiency enhancement in organic solar cells with ferroelectric polymers," Nat. Mater. **10**(4), 296–302 (2011).
23. http://en.wikipedia.org/wiki/Monocrystalline_silicon

1. Introduction

Organic photovoltaic devices have high quantum efficiencies, tunable bandgaps, flexibility and may be manufactured inexpensively [1–3]. However, due to their low carrier-diffusion lengths, the thickness of organic absorbers is typically less than 100nm. This severely limits their absorption of sunlight [1,4,5]. To mitigate this issue, various types of light-trapping schemes that aim to enhance light absorption have been proposed and demonstrated, including dielectric nanostructures [6–8], structured active layers [9,10], and plasmonic nanostructures and concentrators [11–13]. In these studies, the design of the light-trapping structures is performed typically under normal incidence illumination [8,14–16]. Since the performance of most light-trapping schemes deteriorates under oblique incidence, the overall performance of the device is greatly reduced unless expensive solar tracking is implemented. In this article, we apply a modified version of the direct-binary-search (DBS) algorithm to design three-dimensional light-trapping geometries with the specific aim of maximizing the output electric power-density averaged over all possible angles of incidence.

The device under consideration is comprised of an unpatterned active layer sandwiched between two patterned cladding layers. The active layer is a stack of a 20nm-thick PEDOT:PSS layer and a 10nm-thick P3HT:PCBM absorber. The PEDOT:PSS film enhances charge-collection efficiency [17,18]. The cladding layers are made of Gallium Phosphide (GaP), which due to its high refractive index strongly increases the local density of optical states (LDOS) inside the active layer. Increased LDOS allows for an increased number of photonic modes for the incident light to scatter into, which, in turn increases the scattering efficiency and the overall absorption. Four possible configurations of the device are illustrated in Fig. 1. In Fig. 1(a), the top and bottom scattering layers have protrusions, and in Fig. 1(d), both have depressions. In Fig. 1(b), the top scattering layer has a protrusion and the bottom scattering layer has a depression, while the opposite is the case for Fig. 1(c). The bottom-most layer is assumed to be a perfect reflector for simplicity.

The origin of the 3D space is chosen as the center of the top scattering structure (protrusion or depression). Each computational region illustrated in Fig. 1 is assumed to be periodic in both X and Y directions. Overall, there are 12 geometric parameters that may be varied during optimization. These include the periods L_x and L_y, fill factors of the scattering structures, ff_1, ff_2, ff_3 and ff_4, shifts of the bottom scattering structure with respect to the center, S_1 and S_2, thicknesses of the scattering layers, H_{S1} and H_{S2}, and thicknesses of the unpatterned portions of the cladding layers, H_{c1} and H_{c2}.
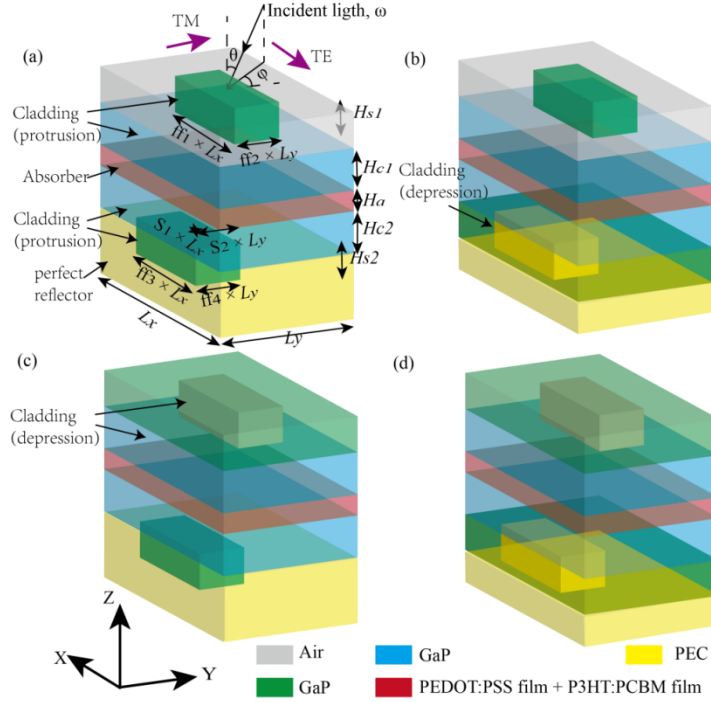
Fig. 1. Device geometries considered in this paper. (a) type 1, (b) type 2, (c) type 3, (d) type 4. See text for details. ω, θ, φ represents the angular frequency of incident light, polar angle and azimuthal angle, respectively. PEC = perfect-electric conductor. TE and TM polarizations are defined as shown by the directions of the electric field vectors.

2. Optimization process and figure-of-merit calculation

For each geometry shown in Fig. 1, the optimization process begins with a random set of values for the 12 parameters mentioned above. The range and unit perturbation for each parameter are listed in Table 1. A free Rigorous Coupled Wave Analysis (RCWA) simulation software package developed at Stanford named S4 was used to compute the absorption spectrum of the active layer. Oblique incident light with AM1.5 spectrum was assumed to be the source. The angle of incidence was varied for the polar angle from −90° to 90° and for the azimuthal angle from −23.5° to 23.5°. For each incident angle, the peak power-density of the device was computed using the absorption spectrum calculated using RCWA. The current-density vs voltage (J-V) curve was first calculated using the detailed balance equations under the assumption of low nonradiative recombination losses [14]. Previous work [6,15,19] has shown that the assumption of low nonradiative recombination losses in ultra-thin (~10nm) organic solar cells is reasonable in investigating the light-trapping effect in organic solar cells.

$$j(V) = q(F_s - F_{co} \exp(\frac{qV}{kT_c})). \tag{1}$$

Here, F_s is the radiative generation rate and is calculated by:

$$F_s = \int_{\omega_g}^{\infty} d\omega S(\omega) A(\omega, \theta = 0, \varphi = 0), \tag{2}$$

where $S(\omega)$ is the incident photon rate per unit bandwidth per unit area at frequency ω, $A(\omega, \theta, \varphi)$ is the absorption spectra of the absorber layer averaged over the two orthogonal polarizations, θ and φ are the incident polar and azimuthal angles, respectively (see Fig. 1(a)),

and ω_g is the absorber's bandgap frequency. The radiative recombination rate, F_{co} is calculated as:

$$F_{co} = \int_0^{2\pi} d\phi \int_0^{\pi/2} d\theta \int_{\omega_g}^{\infty} d\omega \Theta(\omega) A(\omega,\theta,\varphi) \cos(\theta) \sin(\theta), \qquad (3)$$

where $\Theta(\omega) = \dfrac{\omega^2}{4c^2\pi^3}[\exp(\dfrac{\hbar\omega}{kT_c})-1]^{-1}$ is given by planck's law for the radiative spectral photon flux density from the device (treated as a blackbody at a temperature T_c), c is the light speed in vacuum, and $\hbar$ is the reduced Planck's constant.

Then the electric power density is calculated as:

$$P(V) = j(V) \cdot V. \qquad (4)$$

From Eq. (4), the peak power-density is easily obtained.

From Eq. (1) the open-circuit voltage, V_{oc} is given by:

$$V_{oc} = \frac{kT_c}{q} \log\left(\frac{F_s}{F_{co}}\right). \qquad (5)$$

The short-circuit current density, J_{sc} is easily obtained by setting $V = 0$ in Eq. (1):

$$J_{sc} = q(F_s - F_{co}). \qquad (6)$$

The figure-of-merit (FOM) for optimization was the peak power-density averaged over all the incident angles. That is to say, the peak power-density at each incident polar angle (−90° to 90°) and azimuthal angle (−23.5° to 23.5°) is calculated and then averaged to calculate the figure-of-merit (FOM). The sampling steps for the polar and the azimuthal angles are 5° and 3°, respectively. However, our optimization method is also open to a more complicated FOM calculation, for example a weighted average to take into account the solar radiation changes over a calendar year for a certain geographic location. During the optimization, each variable was perturbed by a small positive pre-determined value (as listed in Table 1). Then, the FOM was re-evaluated. If the FOM improved, the perturbation was retained. If the FOM decreased, then the positive perturbation was discarded. A negative perturbation would then be applied and the FOM re-evaluated. One iteration was completed after all the parameters were perturbed in this manner. Then the iterations were repeated until the FOM converged to a stable value. This is the modified version of the direct-binary-search (DBS) algorithm. We repeated the optimization process with a number of random initial solutions, since the algorithm is known to be sensitive to the starting point [6,19,20]. The optimal design with the largest FOM was picked for analysis.

Table 1. Ranges and unit perturbations of geometric parameters for optimization

Parameter	Range	Unit Perturbation
L_x	100nm~1000nm	10nm
L_y	100nm~1000nm	10nm
ff_1	0.00~1.00	0.01
ff_2	0.00~1.00	0.01
ff_3	0.00~1.00	0.01
ff_4	0.00~1.00	0.01
S_x	−0.50~0.50	0.01
S_y	−0.50~0.50	0.01
H_{c1}	0~500nm	5nm
H_{c2}	0~500nm	5nm
H_{s1}	0~500nm	5nm
H_{s2}	0~500nm	5nm

3. Optimization results

The optimized devices of the four types are shown in Figs. 2(a)-(d). Cross-sections through the middle of the bottom scattering layers are shown below each design. The labeled dimensions are in nanometers and the figures are not drawn to scale. The absorption spectra of each device averaged over all the angles of incidence are shown in Figs. 2(e)-(h) for TE (red), TM (blue) and unpolarized (black) light. The absorption spectrum (purple) for a reference device with a planar absorber sandwiched between a top anti-reflection coating (ARC) and a perfect back reflector is shown for comparison.
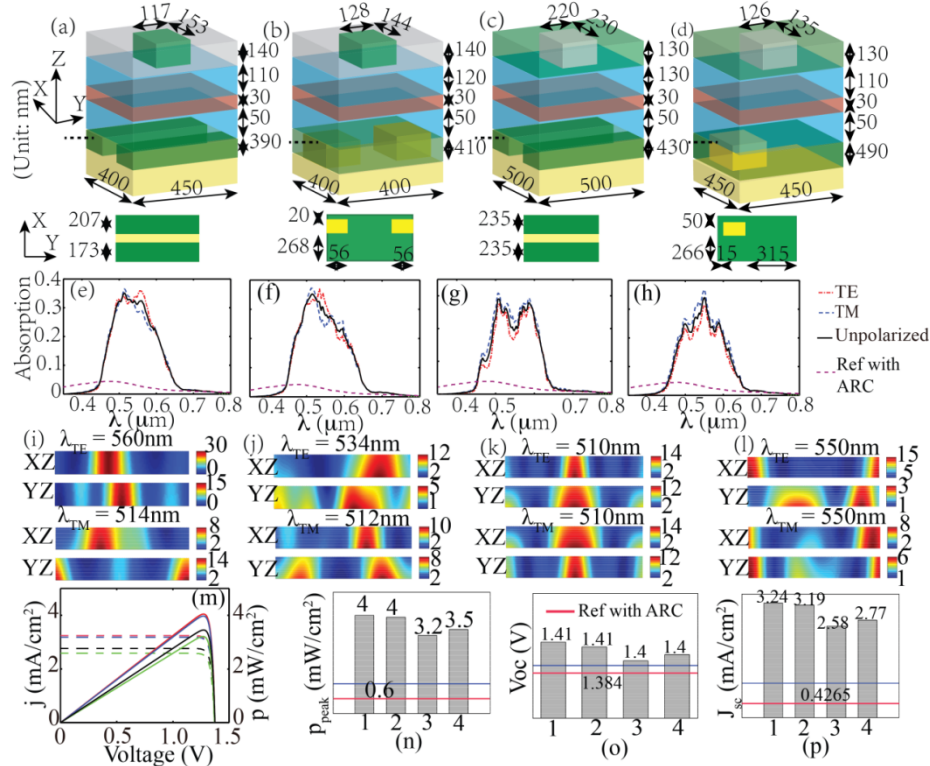

Fig. 2. Optimized devices for type 1 (a), 2 (b), 3(c) and 4(d). Cross-sections through the bottom scattering layers are shown below each type. Dimensions are in nm and the figures are not to scale. Absorption spectra averaged over all angles of incidence (polar angle from −90° to 90° and azimuthal angle from −23.5° to 23.5°) of the corresponding devices are in (e)-(h). Red and blue dashed lines correspond to TE and TM polarizations, respectively. The black solid lines correspond to unpolarized illumination (average of TE and TM). Absorption spectrum of the reference device with ARC is shown by purple dashed lines. Field-intensity distributions in the active layer under normal incidence for certain absorption resonant peaks are shown in (i)-(l). The field patterns labeled with XZ gives the electric field distribution in the XZ plane at Y = 0. A similar definition applies to the field patterns labeled with YZ. The J-V curves again averaged over all angles of incidence are shown in (m). Comparisons of the peak power-densities, open-circuit voltages and short-circuit current-densities for all devices are shown in (n), (o) and (p), respectively. In each figure, the reference device with ARC is denoted by red lines.

The optimized devices show significant increase in absorption compared to the reference planar device with ARC and perfect back reflector. Furthermore, the optimized devices also exhibit numerous sharp spectral peaks. Below ~450nm, the parasitic absorption of GaP lowers the absorption of the active layer. Due to the high index-contrast between the cladding layer of GaP and the active layer of P3HT:PCBM, one can expect strong confinement of the

exited guided modes within the active layer. As has been theoretically proposed [21], the increased LDOS allows for incident light to scatter into many more guided modes, which eventually boosts the light absorption in the active region. To illustrate this point, we plot the light-intensity distributions within the active layer under normal incidence for those wavelengths where absorption is maximum for each polarization in Figs. 2(i)-2(l). The intensities are normalized to incident light intensity, and enhancement and confinement are obvious. These are the result of the excitation of guided modes that are propagating in the plane of the absorber. Videos of the propagation of the fields at wavelengths of peak absorption are included in the supplementary information. The field videos show the excitation of modes that propagate predominantly in the plane of the absorber, thereby drastically increasing their absorption.

The electrical characteristics of the optimized devices are shown in Figs. 2(m)-2(p). The optimized device of type 1 exhibits the highest angle-averaged peak power-density of 4mW/cm^2. This corresponds to a 6.7X enhancement over that of the reference device. Moreover, both the angle-averaged short-circuit current-density and the angle-averaged open-circuit voltage exhibit a significant increase when compared to those of the reference device. The increase in short-circuit current is due to the enhanced absorption, which results in more carriers being generated. The increase in the open-circuit voltage is due to the considerable difference between the total absorption and the absorption at energies immediately above the bandgap of the P3HT:PCBM absorber [14]. The larger this difference, the larger the open-circuit voltage. From the absorption spectra we can see that when compared to the reference device, absorption from 470nm to 600nm is significantly increased, while absorption immediately above the bandgap (~750nm) is about the same.

4. Comparison to device optimized for normal incidence

We have optimized a similar device but only for normal incidence previously. Here, we compare this device to that optimized for oblique incidence (of type 1) to further elucidate the photonic principles of these devices. Figure 3(a) shows the device optimized under normal incidence. Figure 3(b) shows the electrical properties of both devices averaged over all the angles of incidence (polar angle from −90° to 90° and azimuthal angle from 0° to 360°). Clearly, the device optimized with the angles of incidence taken into account shows higher short-circuit current-density and peak power-density.

We also calculated the peak power-density of both devices as a function of the polar and azimuthal angles, and plotted these in Figs. 3(c) (device optimized for normal incidence) and 3(d) (device optimized under oblique illumination). Both devices exhibit little dependence on azimuthal angle. However, as the polar angle increases, the peak power-density decreases (as expected) for both devices. The peak power-density of the device optimized for all angles decreases at a slower rate with polar angle than the other device. However, the trade-off is that the peak power-density at normal incidence for the device optimized for all angles is somewhat smaller compared to the other device. One can define the 3dB polar angle as the polar angle at which the peak power-density falls to half of its maximum value. For the device optimized under normal incidence, the 3dB polar angle is 30°, while that of the device optimized for all angles is ~50°. The peak power-density averaged over all azimuthal angles is plotted against the polar angle in Fig. 3(e). It is clear that although the device optimized under all angles shows lower peak power-density at 0°, over all the polar angles, it has higher average peak power-density. This is further evident in the peak power-density averaged over all polar angles plotted as a function of the azimuthal angle in Fig. 3(f). The variation with azimuthal angle is small and shows interesting effects of symmetry of the scattering structures. Clearly, the device optimized under all angles of incidence has the capability of coupling incident light (from many angles) into guided-modes, which are primarily trapped within the absorber layer.
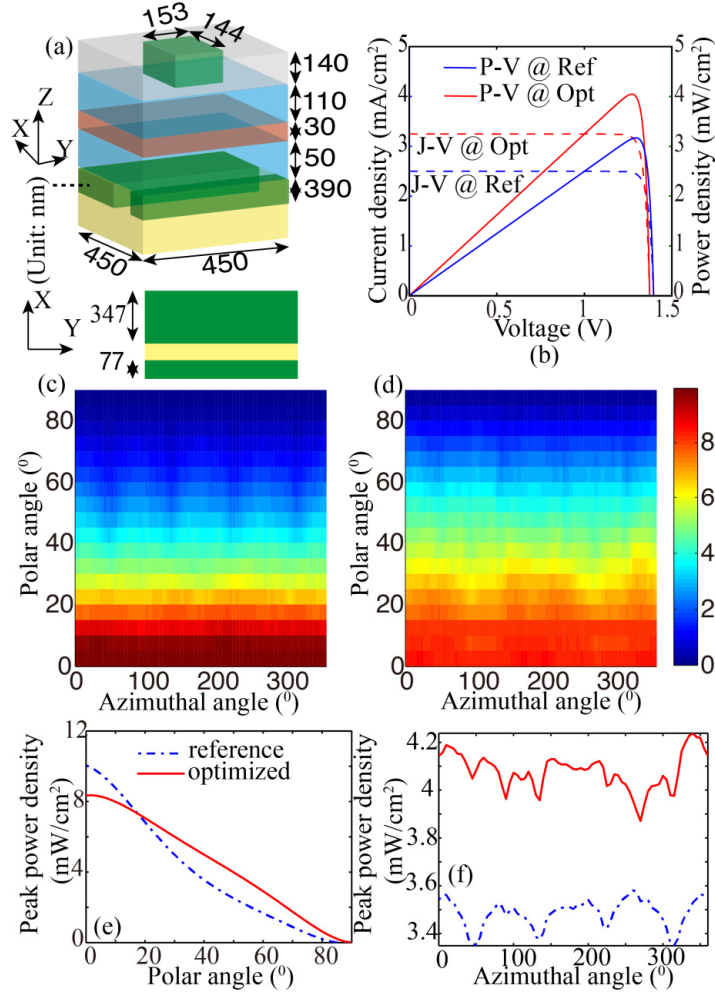
Fig. 3. Comparison of the optimized device of type 1 (from Fig. 2(a)) against a reference device optimized under normal illumination. (a) Geometry of the reference device that is optimized under normal illumination. Cross-section through the bottom scattering layers is shown. (b) The current-density and peak power-density averaged over all angles of incidence as a function of voltage for the optimized device 1 (red) and reference device (blue). (c) and (d) 2D plots of peak power-density as a function of polar angle and azimuthal angle for the reference device and optimized device 1, respectively. (e) Peak power-density as a function of polar angle. (f) Peak power-density as a function of azimuthal angle. Note that for polar angle analysis in (e), we averaged the peak power-density over all azimuthal angles, while for azimuthal angle analysis in (f), we averaged the peak power-density over all polar angles.

We further plotted the absorption spectra under various angles of incidence for both devices in Fig. 4(a). For both devices, a large number of resonance peaks occur around 470nm-600nm, where the slot-waveguide effect is strong and lots of guided-mode resonances exist. The reduced absorption below 450nm is due to the parasitic absorption by the GaP cladding layers. At ~510nm and at small polar angles (e.g. 0°), the absorption spectrum for the device optimized for all angles shows a dip while an absorption peak is clearly observed in the reference device (the one that was optimized for normal incidence). However, at large polar angles (e.g. >30°), the absorption of the optimized device at 510nm is much higher than that of the reference. This is further illustrated by the light-intensity distributions within the active layer at 510nm for different polar angles (Fig. 4(b)). At small polar angles, the electric

field intensity for the reference exhibits strong enhancement over that of the optimized device. The opposite is the case for large polar angles (e.g. 30° and 60°). This suggests that the optimized design boosts absorption at larger angles at the expense of that at normal incidence. This is intuitive since the fraction of the total energy incident at angles larger than 0° is much higher than that incident normally. Most of this trade-off occurs at ~510nm, which corresponds to the peak of the AM1.5 spectrum.
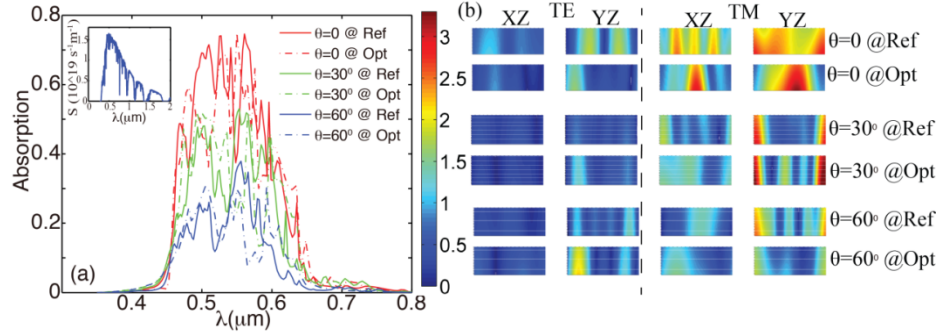

Fig. 4. (a) Impact of incident polar angle on absorption spectrum of the reference structure and the optimized structure 1. Solar photon flux as a function of wavelength is shown in the inset. The absorption spectra are taken at an azimuthal angle of 0°. (b) Field patterns for the reference device and optimized device 1 under the polar angle of 0°, 30°, and 60°, respectively. The field patterns in "XZ" column are taken in the XZ plane at Y equals zero, while the field patterns in "YZ" column are taken in the YZ plane at X equals zero. All the field patterns are calculated at zero azimuthal angle.

5. Total energy generated in a year

To illustrate the excellent performance of the optimized structure in a realistic situation, we calculated the total energy-density generated by the device in one year. Also, the accumulated energy-density for the reference (device optimized under normal illumination) and a planar solar cell with a conventional anti-reflection coating (ARC) are also shown for comparison. The planar solar cell with a 20nm-thick PEDOT:PSS layer and a 10nm-thick P3HT:PCBM absorber is sandwiched between a perfect back reflector and a 30nm-thick indium tin oxide (ITO), which acts as the ARC. We assume that the device is located at the equator and only direct sunlight is considered. For the calculation, the polar angle varies form −90° to 90°, representing the daily motion of the sun, and the azimuthal angle from 23.5° to 23.5°, representing the seasonal variation of the sun. For structure 1 (the best device optimized over all angles), the total annual energy-density generated is 62.9KJ/cm^2, which represents a 1.25X and 7.23X enhancement over that generated by the reference (optimized for normal incidence) and by the planar solar cell with ARC, respectively.

In addition, we also calculated a comparison between the device proposed in this article and a state of art P3HT solar cells with a 150nm-thick absorber. The annual energy of a P3HT solar cell is estimated as follows. It has been widely reported that the total energy generated by a typical monocrystalline silicon solar cell during a day is 0.144 KJ/cm^2. The state of art organic solar cells' efficiency with a 150nm-thick P3HT absorber is reported to be ~8% [22] and this corresponds to ~38% of the efficiency of a monocrystalline silicon solar cell (assuming that the silicon cell efficiency is 21% [23]). As a result, the total energy generated by the P3HT solar cell in one year is estimated to be ~19.7 KJ/cm^2. Compared to this, our optimized device produces on average ~3.2 times more energy per year.

6. Conclusion

In this paper, we presented the application of a modified version of the direct-binary-search (DBS) algorithm to design 3D nanophotonic light-trapping to maximize the peak power-

density from ultra-thin organic solar cells under oblique illumination. High-index GaP was exploited as the cladding material in order to increase the LDOS and thereby increase the trapping efficiency.

The optimized device produced an averaged peak power-density of 4mW/cm^2 when the polar angle was varied from −90° to 90° and the azimuthal angle was varied from −23.5° to 23.5°. This was much higher than that produced by a reference device with ARC and back-reflector (0.6mW/cm^2). We performed a careful analysis of the performance of this device as well as a similar device optimized for normal illumination. Lowering the absorption at normal incidence is essential to enhance absorption at other angles of incidence. This is particularly evident ~510nm (the peak of the solar spectrum). We further show that by explicitly optimizing devices for operation under various angles of incidence, it is possible to generate significantly higher energy without tracking the sun. Specifically, we show that our optimized device produces 7.23X more energy than a planar device (with a conventional ARC) over the course of a year without any sun tracking. Although the example of organic absorbers and dielectric cladding layers were used here, our method can be readily applied to other materials including plasmonic scatterers. More generalized geometries may also be readily incorporated to provide improved performance [19].